THE ASTROPHYSICAL JOURNAL, 472:571–581, 1996 December 1

REPROCESSING MODELS AND THE *ADVANCED SATELLITE FOR COSMOLOGY AND ASTROPHYSICS* SPECTRUM OF MARKARIAN 290

T. J. TURNER,[1,2] I. M. GEORGE,[1,2] T. KALLMAN,[1] T. YAQOOB,[1,2] AND P. T. ŻYCKI[3]

Received 1996 January 29; accepted 1996 June 12

ABSTRACT

We present the results from a 40 ks *Advanced Satellite for Cosmology and Astrophysics* observation of the Seyfert 1 galaxy Mrk 290. The source is found to have a complex spectral form, with emission and absorption features caused by oxygen and iron superimposed on an underlying power-law continuum with photon index ~ 1.9 Mrk 290 is also found to exhibit significant flux-correlated spectral variability, predominantly below 2 keV, on a timescale of $\sim 5 \times 10^4$ s.

The relatively strong spectral features observed in this source make it an interesting case to use for an investigation of models for reprocessing of the X-ray continuum by ionized material. We consider ionized reprocessors based on the XSTAR photoionization code for geometries in and out of the line of sight. Models in either geometry provide a vast improvement over a simple absorbed power-law model.

The warm absorber/emitter model provides a good explanation of the overall spectral shape, with a column density of $N^{*}_{\mathrm{H},z} \sim 8 \times 10^{21}$ cm^{-2} of ionized material (ionization parameter $\xi = 24$) most likely within $\sim 10^{17}$ cm of the central source. While the data do not allow us to unambiguously determine the origin of the spectral variability, it is consistent with a drop of $\sim 25\%$ in flux accompanied by a proportional drop in the ionization state of the warm absorber. The intense Kα line of equivalent width ~ 500 eV present in the source can be modeled as a broad Gaussian of FWHM ~ 0.5 keV, or by a line profile expected from the inner regions of a relativistic accretion disk inclined at $\sim 30°$. In both cases, the rest-frame line energy is consistent with weakly ionized iron and cannot be explained by the warm emitter.

An ionized reflector can also model the overall spectral shape, yielding $\xi_{\mathrm{ref}} \sim 80$, although it has some difficulty simultaneously fitting both the iron Kα line and the soft X-ray spectral features. This model offers no simple explanation for the observed spectral variability, and the intensity of the reflected component is greater than that expected from a semi-infinite slab illuminated by an isotropic source.

A hybrid model featuring reprocessing in both the warm absorber/emitter and reflector may be the most realistic scenario. In this case, the preferred fit models the soft X-ray regime (and spectral variability) with the warm absorber/emitter and the iron Kα line with a weakly ionized reflector ($\xi \lesssim 20$).

Subject headings: galaxies: individual (Markarian 290) — galaxies: nuclei — radiation mechanisms: thermal — radiative transfer — X-rays: galaxies

1. INTRODUCTION

Ginga observations of active galactic nuclei (AGNs) in the 2–20 keV band revealed iron Kα emission lines and edges in the $\sim$6–8 keV band, as well as a spectral flattening above ~ 10 keV (Pounds et al. 1990; Nandra & Pounds 1994). These observations provided strong evidence that a significant fraction of the AGNs continuum radiation is reprocessed, although the location, geometry, and ionization state of the reprocessing material are not fully understood.

While some X-ray line emission is expected from the ionized line-of-sight material (the "warm absorber")—thought to exist in many Seyfert type AGNs (e.g., Halpern 1984; Netzer 1993; Fiore et al. 1993)—physically plausible models of the warm absorber appear unable to produce the relatively high equivalent widths typically observed ($\sim$150–200 eV) in iron Kα (Nandra & Pounds 1994; Matt 1994).

However, placing the reprocessing material out of the line of sight in the popular "reflection" models (Lightman & White 1988) predicts equivalent widths much closer to those observed (George & Fabian 1991; Matt, Perola, & Piro 1991). Such models have the primary X-rays reprocessed (or "reflected") in optically thick material subtending a substantial solid angle to the X-ray source, possibly the putative accretion disk. If the disk is neutral, photoelectric absorption by carbon, nitrogen, and oxygen means there is little reflection at low energies. However, as the lighter elements become ionized, reflection and line emission at soft X-ray energies become important (Ross & Fabian 1993; Matt, Fabian, & Ross 1993; Życki et al. 1994). Iron is the most abundant heavy element and can give rise to strong emission lines between the two extremes of 6.4 keV fluorescence (from neutral material) and 6.97 keV recombination line (from ionized material). Iron K shell absorption edges between 7.1 and 9.3 keV might also be expected. Such features have been observed in *Ginga* and other data (e.g., Nandra & Pounds 1994 and references therein). Applying the reflection model to the *Ginga* data yielded intrinsic continuum photon indices of $\Gamma \sim 1.9$ (Nandra & Pounds 1994) for Seyfert 1 galaxies.

Mrk 290 is a radio-quiet Seyfert 1 galaxy of low redshift ($z = 0.029$; Markarian 1969), which was first detected as an X-ray source by *HEAO 1* (Wood et al. 1984) and subsequently observed by the *Einstein Observatory* (Kriss, Canizares, & Ricker 1980; Kruper, Urry, & Canizares 1990) and *EXOSAT* (Turner & Pounds 1989; Ghosh & Soundararajaperumal 1992). Ghosh & Soundararajaperumal reported the significant detection of an iron Kα emission line in the source, with a remarkable equivalent width of

[1] Laboratory for High Energy Astrophysics, Code 660, NASA/Goddard Space Flight Center, Greenbelt, MD 20771.
[2] Universities Space Research Association.
[3] Nicolaus Copernicus Astronomical Center, Bartycka 18, 00-716, Warsaw, Poland.

$1.2^{+0.9}_{-0.8}$ keV. Despite the unsuitability of the *EXOSAT* medium- and low-energy instruments to a study of spectral features, the result appears to be very significant, suggesting Mrk 290 contains one of the strongest iron lines ever observed in a Seyfert 1 galaxy.

In § 2, we present an *Advanced Satellite for Cosmology and Astrophysics* (*ASCA*) observation of Mrk 290 and describe the data reduction techniques used. Preliminary results presented in § 3 show that the X-ray spectrum of this source is complex and variable. We explore the spectral variability in the context of models in which the primary continuum is reprocessed by ionized material in and out of the line-of-sight in § 4 and § 5, respectively. These results are then discussed in § 6, along with a hybrid model. We present our conclusions in § 7.

2. THE *ASCA* OBSERVATION AND DATA REDUCTION

The observation reported here was carried out by the (*ASCA*) over the period 1994 June 15–16. *ASCA* has four instruments covering the 0.4–10 keV X-ray energy band (Tanaka, Inoue, & Holt 1994): two solid-state imaging spectrometers (SIS), each consisting of 4 CCD chips yielding ~2% energy resolution at 6 keV; and two gas imaging spectrometers (GIS) of energy resolution ~8% at 6 keV. The SIS data were obtained using 2 CCD readout mode, whereby 2 CCD chips are exposed on each SIS with the target at the nominal pointing position. A mixture of "FAINT" and "BRIGHT" SIS telemetry modes were used, but the data were combined by converting the "FAINT" mode into "BRIGHT," increasing the signal-to-noise ratio by incorporating more data.

The following data-selection criteria were applied: the spacecraft was outside of the South Atlantic Anomaly; the elevation angle above the Earth's limb was greater than 5°; the Bright Earth angle (elevation angle above the Sun-illuminated Earth's limb) was greater than 20°; the magnetic cut-off rigidity was greater than 6 GeV c^{-1} for SIS data and greater than 7 GeV c^{-1} for GIS data. "Hot" and "flickering" pixels were removed from the SIS using an algorithm excluding pixels showing count rates outside of the expected Poissonian distribution. SIS grades 0, 2, 3, and 4 were selected for the analysis. After these screening criteria had been applied, we extracted a light curve for each instrument and manually removed time bins containing spikes caused by high background, as well as a short period of unstable pointing prior to target aquisition. These selection criteria in an effective exposure time of ~40 ks in each of the four detectors.

As mentioned above, and confirmed in § 3, Mrk 290 exhibits a strong iron Kα emission line in the 6.4–7.1 keV band. The parameters of the line are reasonably well determined in the GIS data, and therefore we used this feature to determine the gain of the SISs. We fit the SIS and GIS data above 4 keV with a power-law model plus a narrow Gaussian line. Comparison of the best-fit line energies in the four instruments revealed that during our observation the GISs were in good agreement, but that the gain of SIS0 and SIS1 were at 96.7% and 94.9% of their nominal values, respectively. These values were used to correct the SIS data throughout. As a cross-check of the spectral results, we also populated the SIS pulse-invariant (PI) column in the event file and reextracted the source spectra. Consistent results were obtained using both methods.

We note that there are a few remaining uncertainties associated with the SIS calibration, and these will be discussed at an appropriate places in the text below.

3. PRELIMINARY RESULTS

Mrk 290 was detected in all four instruments, with no evidence for any nearby (contaminating) source. Images were extracted from the screened and cleaned data from all instruments, and region descriptors were defined for extracting light curves and spectra. Circular extraction cells of ~4′ (SIS) and ~6′ (GIS) radius centered on Mrk 290 were used, with corresponding background regions defined in source-free areas of the same SIS CCD chip or the same GIS. The mean background-subtracted count rates were 0.319 ± 0.003 and 0.253 ± 0.003 counts s^{-1} in SIS0 and SIS1, respectively, in the 0.4–10 keV band, and 0.181 ± 0.002 and 0.220 ± 0.003 counts s^{-1} in GIS2 and GIS3, respectively, in the 0.8–10 keV band. Assuming the best-fitting spectral models discussed below, the mean fluxes during this observation were $F_{0.5-2} = 3.9 \times 10^{-12}$ ergs cm^{-2} s^{-1} and $F_{2-10} = 8.4 \times 10^{-12}$ ergs cm^{-2} s^{-1} in the 0.5–2 keV and 2–10 keV bands, respectively, corresponding to observed luminosities[4] of $L_{0.5-2} = 7.3 \times 10^{42}$ ergs s^{-1} and $L_{2-10} = 1.6 \times 10^{43}$ ergs s^{-1}.

All instruments showed Mrk 290 to have varied in flux during the *ASCA* observation. Figure 1 shows the SIS0 light curves in the 0.4–2 keV and 2–10 keV bands. The points in the light curve were computed from the count rates in the final good-time intervals, so the bin size is variable, ranging from ~300 to 2000 s, and significant variations are evident in both bands. Consistent behavior was observed in the other detectors.

Given the variability of Mrk 290 during the observations, here and in the following sections we consider three spectra: (1) the mean spectrum, extracted from the entire observation; (2) the high-state spectrum, extracted from the first ~50 ks baseline of the observation; and (3) the low flux state spectrum, extracted from the second ~50 ks baseline of the observation. (The high/low state division is also noted on Fig. 1). All model spectra are corrected for photoelectric absorption, parameterized by an effective hydrogen column density N_H, assuming the cross sections and abundances given by Morrison & McCammon (1983). The column density of neutral material was constrained to be greater than the Galactic 21 cm value, $N_{H,0}^{21} = 1.76 \times 10^{20}$ cm^{-2} (Stark et al. 1992). In all cases, spectral analysis is performed on the data from all four instruments simultaneously, with different relative normalizations to account for (small) uncertainties in the determination of their effective areas and some uncertainty in the loss of counts from each individual extraction cell. For fits to the mean spectrum in which all the parameters were free (Tables 1, 2, and 3), the relative normalizations were also allowed to vary. These fits to the mean spectrum allow the best determination of the relative levels of the four instruments, and as the same extraction cells were used for the mean, high, and low state spectra, these normalization factors were fixed in all ensuing fits. As there is some uncertainty in the detailed calibration of the SIS below 0.6 keV, we have added a systematic error of 20% to SIS channels below 0.6 keV. This is much larger than the uncertainty in those channels (and we also confirmed that consistent results were obtained if the data

[4] $H_0 = 70$ km s^{-1} Mpc^{-1} and $q_0 = 0.5$, assumed throughout.

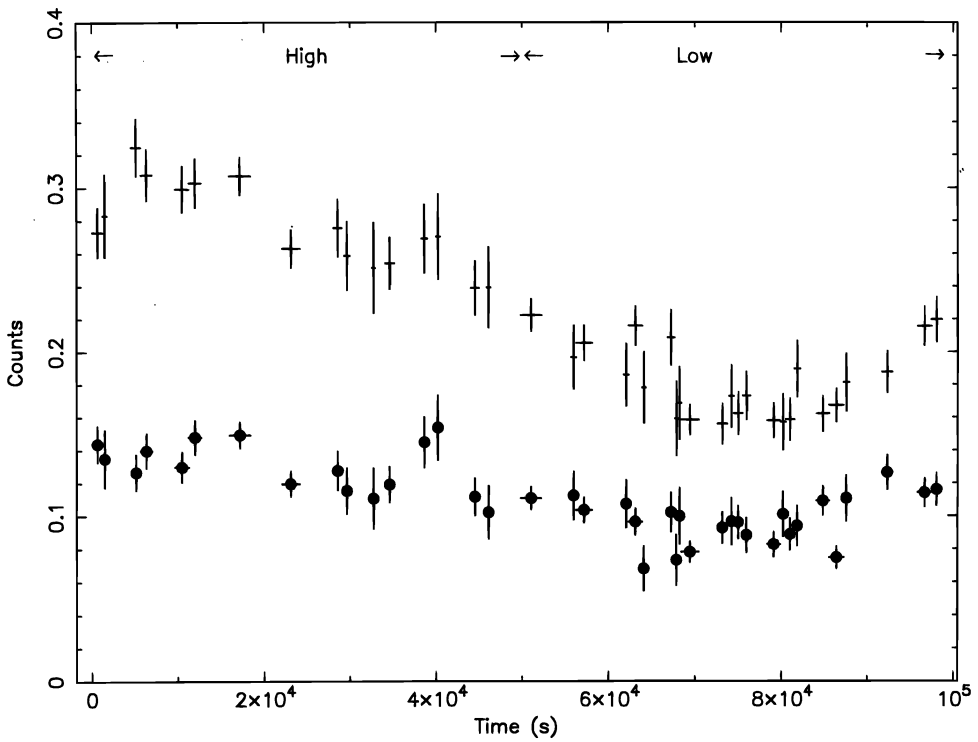

FIG. 1.—SIS light curves from the *ASCA* observation of Mrk 290 carried out 1994 June 15–16. Bin size is variable, ranging from 300–2000 s. Division between high and low state (as defined for this observation) is noted on the plot. Large filled circles (*bottom*) represent the 2–10 keV light curve, the smaller circles (*top*) represent the 0.4–2 keV light curve.

below 0.6 keV were dropped from the analysis). As the low-energy data are so remarkable, we examined the *ROSAT* PSPC spectrum of Mrk 290. The soft X-ray features evident in Figure 2 are highly significant in the PSPC spectrum, confirming that these features are not an artifact of any SIS calibration problem.

First, we consider a simple power-law model applied to the mean spectrum: this did not provide an adequate fit to the data (Table 1) with a χ^2 statistic of 1018 for 791 degrees of freedom (dof). An excess is clearly visible in the data/model ratio in the 6–7 keV band (Fig. 2) indicative of iron Kα emission, which is commonly seen in Seyfert galaxies (Nandra & Pounds 1994; Mushotzky, Fabian, & Iwasawa 1995). The residuals seen in the 0.4–2 keV regime are also commonly seen in Seyfert galaxies (e.g. Nandra & Pounds 1992), although the features are unusually strong in Mrk 290. It is widely thought that these features are indicative of reprocessing in ionized material.

We now consider the simple power-law model applied to the high and low state spectra. From Table 1 it can be seen that best-fitting power-law normalization $A_{\rm pl}$ and photon index (Γ) decrease between the high state and low state, as expected from Figure 1. In § 4, we investigate two self-consistent models for reprocessing by ionized material in and out of the line of sight.

We constructed a "difference spectrum" by subtracting the low state spectrum in each instrument from the high state spectrum (Fig. 3). This shows that the source counts vary significantly up to at least 5 keV (and there is a hint of iron line variability). Absorption effects are only significant up to 2 keV in this source; thus, not all the observed variability can be explained simply by variations in absorption alone. Hence, in the ensuing study of the spectral variability, we always allow the normalization of the power-law component to vary. Fitting the "difference spectrum" with a power law absorbed by the Galactic column yielded a good fit with $\Gamma = 1.97 \pm 0.09$ and $\chi^2 = 724$ for 731 dof.

4. REPROCESSING BY IONIZED MATERIAL ALONG THE LINE OF SIGHT

Our models for X-ray line emission and partially ionized absorbers are calculated using the XSTAR photoionization code (Kallman & Krolik 1995). The code has some updates since Kallman & Krolik, which are summarized in the Appendix along with further details of the code.

In brief, a series of XSTAR models were run for slabs of

TABLE 1

POWER-LAW FITS TO THE *ASCA* OBSERVATION OF MRK 290

Parameter	Mean	High State	Low State
$A_{\rm pl}$ (10^{-3} keV cm^{-2} s^{-1} keV^{-1}).....	$1.75^{+0.07}_{-0.08}$	$2.15^{+0.11}_{-0.10}$	$1.41^{+0.09}_{-0.02}$
Γ.....	1.57 ± 0.03	1.63 ± 0.04	$1.49^{+0.05}_{-0.03}$
$N_{\rm H,0}$ (10^{21} atom cm^2)	$0.17 < 0.11$	$0.0 < 0.10$	$0.0 < 0.09$
χ^2_r (dof).....	1018 (791)	833 (731)	760 (620)

NOTE.—Errors are for $\pm$90% confidence for one interesting parameter ($\chi^2_{\rm min} + 2.71$).

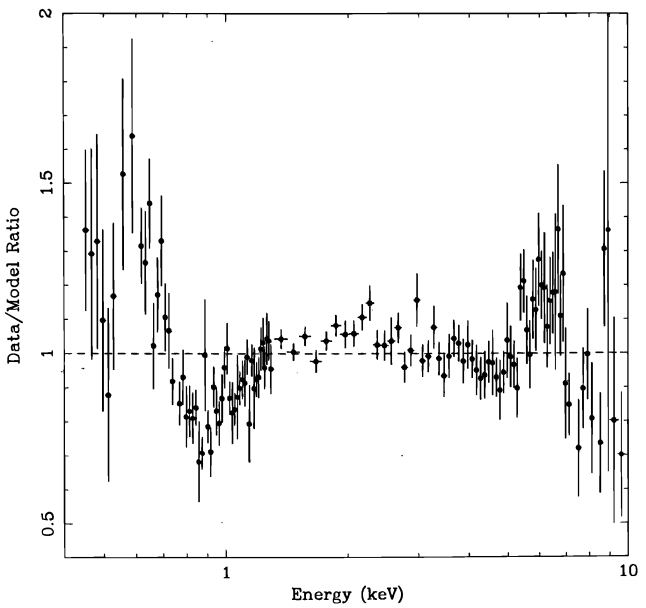

FIG. 2.—Data/model ratio after fitting of the simple power-law model to the mean spectrum of Mrk 290 (Table 1). SIS and GIS data have been combined so that the deviations from the model can clearly be seen. Same features are present in each individual dataset.

gas (of density n, and column density $N^*_{\mathrm{H},z}$) illuminated by ionizing spectra (parameterized by the ionization parameter at the illuminated face ξ, defined in eq. [A3]). The code simultaneously determines the ionization state of the gas and the local radiation field as a function of position in the slab. The state of the gas at each position follows from the assumption of a stationary local balance between heating and cooling and between ionization and recombination. In all cases considered in this section, n was fixed at 10^{10} cm^{-3} and the ionizing continuum was a single power law of photon index $\Gamma = 1.9$. The output from each run consists of the predicted transmitted spectrum (of the ionizing continuum), along with the predicted emission spectrum of the gas (consisting of line emission and recombination continua). In the spectral analysis, the normalization of the emission spectrum was allowed to be free; this quantity was used to estimate the covering fraction of the ionized material (see Appendix, eq. [A2]). A grid of such models was constructed (covering a range of ξ and $N^*_{\mathrm{H},z}$ applicable to the source), and the resultant model spectra was used during spectral analysis.

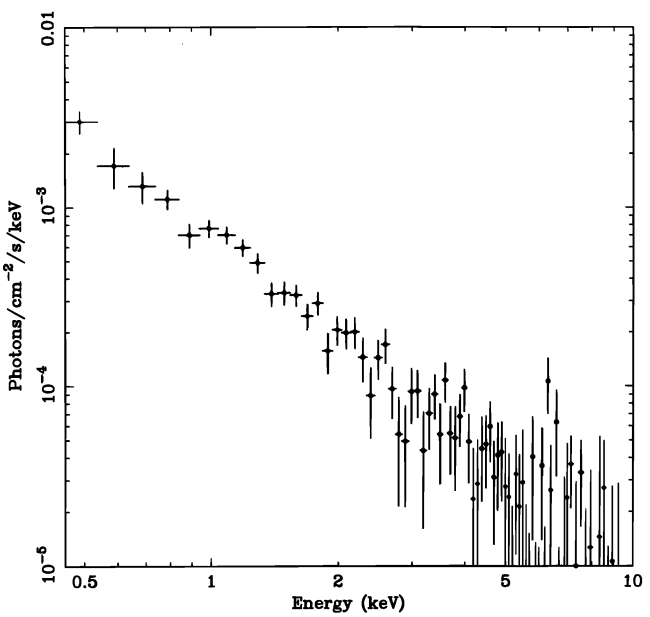

FIG. 3.—The "difference spectrum" between the high and low states displayed in summed flux for the four *ASCA* instruments. Low-state spectrum was subtracted from the high-state spectrum for each of the four instruments; the resultant "difference spectra" were added together for illustration.

4.1. *The Mean Spectrum*

We fit the mean spectrum, assuming a model composed of a power-law continuum absorbed by a column of ionized material (as described above), where the column $N^*_{\mathrm{H},z}$ is assumed to be at the redshift of the source. In addition, we allowed a neutral column at zero redshift, constrained to be at least as large as $N^{21}_{\mathrm{H},0}$. As the strength of the iron Kα emission line exceeds that predicted by such models, we also allowed a Gaussian emission line (at an energy E^l_z in the rest frame of the source, and width σ^l_z).

The results of this fit are listed in Table 2A, and the best-fit model is shown in Figure 4, along with the data/model ratio. Comparison of Figures 2 and 4 illustrate the significant improvement in overall fit obtained with such a model. Specifically, the excess in the data/model ratio seen in Figure 2 below ~ 0.7 keV is accounted for by the "warm emitter," the deficit in the 0.7–1.5 keV band apparent in Figure 2 is explained by the "warm-absorber," and the excess in the iron K band is accounted for by the Gaussian emission line. While this model obviously fits the overall spectrum quite well (c.f. Fig. 2), there remain a few data/model deviations across the *ASCA* bandpass. Most notably, the ratio deficit close to 1.7 keV arises as a result of the model prediction of significant silicon line emission, which is not observed.

The best-fitting rest energy of the iron Kα line is $E^l_z = 6.33 \pm 0.16$ keV, consistent with emission from neutral iron. Recent *ASCA* observations of other Seyfert galaxies have shown that the iron Kα emission line is often significantly broad, with FWHM up to $\sim 10^5$ km s^{-1} (e.g. Mushotzky et al. 1995; Tanaka et al. 1995; Yaqoob et al. 1995; Nandra et al. 1996). Indeed, the width of the line in Mrk 290 significantly exceeds the instrument resolution (even given the broadening of the SIS response at this epoch), yielding $\sigma^l_z = 0.53^{+0.21}_{-0.17}$ keV. We caution that in these data we have almost no constraint on the continuum above the iron K line, because of the reduction in signal-to-noise above 7 keV, therefore stringent constraints cannot be obtained on the line width. The constraints on line width indicate FWHM velocities of 17,000–34,000 km s^{-1} (at 90% confidence) if the width of the line is caused by Doppler shifts. The line width—and therefore the implied velocity range—is similar to that observed for many Seyfert galaxies. The line equivalent width of 492^{+176}_{-149} eV exceeds that expected from a warm absorber by a large factor. Thus, we assume the observed line is predominantly emitted from another location. The mean spectrum was also fitted with an emission line profile of the form expected from the inner regions of a relativistic accretion disk (using the warm absorber model in Table 2A, but replacing the broad Gaussian component with the disk-line component). Such a profile has been suggested in NGC 3227 (George, Nandra, & Fabian 1990) and recently confirmed in MCG−6-30-15

TABLE 2

WARM ABSORBER FITS TO THE *ASCA* OBSERVATION OF MRK 290

Parameter	Mean	High State	Low State
A. Power Law with Ionized Absorber			
A_{pl} (10^{-3} keV cm^{-2} s^{-1} keV^{-1}	$2.76^{+0.34}_{-0.19}$	$3.03^{+0.32}_{-0.20}$	$2.13^{+0.33}_{-0.21}$
Γ.....	$1.86^{+0.08}_{-0.06}$	$1.89^{+0.14}_{-0.06}$	$1.79^{+0.09}_{-0.08}$
$N_{H,0}$[a] (10^{21} atom cm^{-2})	$0.18^{+0.13}_{-0.06}$	$0.25^{+0.51}_{-0.10}$	$0.26^{+0.39}_{-0.18}$
$N^{*}_{H,z}$ (10^{21} atom cm^{-2}).....	$7.94^{+4.78}_{-1.32}$	$4.95^{+6.30}_{-1.44}$	$6.23^{+5.0}_{-2.1}$
ξ (ergs s^{-1} cm).....	24^{+18}_{-6}	20^{+35}_{-10}	16^{+18}_{-3}
C_{XSTAR}[b] (%).....	88^{+75}_{-74}	79^{+108}_{-60}	101^{+100}_{-97}
E^{I}_{z} (keV).....	6.33 ± 0.16	$6.34^{+0.28}_{-0.33}$	$6.30^{+0.18}_{-0.17}$
σ^{I}_{z} (keV)	$0.53^{+0.21}_{-0.17}$	$0.60^{+0.21}_{-0.22}$	$0.52^{+0.21}_{-0.16}$
A^{I}_{z} (10^{-5} photons cm^{-2} s^{-1})	$4.48^{+1.47}_{-1.49}$	$4.73^{+3.65}_{-2.92}$	$6.00^{+1.92}_{-2.51}$
EW (eV)	492^{+176}_{-149}	468^{+328}_{-202}	739^{+195}_{-221}
$F_{0.5-2}$ (10^{-12} ergs cm^{-2} s^{-1})	3.9	4.7	3.2
F_{2-10} (10^{-12} ergs cm^{-2} s^{-1})	8.4	9.4	7.6
χ^2_r (dof).....	845 (785)	767 (722)	650 (611)
B. Variable Γ and A_{pl}			
A_{pl} (10^{-3} keV cm^{-2} s^{-1} keV^{-1}	...	3.42 ± 0.09	2.17 ± 0.06
Γ.....	...	1.94 ± 0.03	1.79 ± 0.03
A^{I}_{z} (10^{-5} photons cm^{-2} s^{-1})	...	$5.69^{+2.50}_{-2.01}$	$5.79^{+0.71}_{-2.54}$
χ^2_r (dof).....	...	781 (725)	652 (615)
C. Variable Ionization Parameter and A_{pl}			
A_{pl} (10^{-3} keV cm^{-2} s^{-1} keV^{-1}).....	...	3.16 ± 0.08	2.33 ± 0.06
ξ (ergs s^{-1} cm)	...	$31.6^{+6.5}_{-5.8}$	$18.3^{+3.1}_{-2.0}$
A^{I}_{z} (10^{-5} photons cm^{-2} s^{-1})	...	$4.40^{+0.48}_{-3.08}$	$7.04^{+1.34}_{-2.11}$
χ^2_r (dof).....	...	782 (726)	653 (615)
D. Variable Warm Column and A_{pl}			
A_{pl} (10^{-3} keV cm^{-2} s^{-1} keV^{-1}).....	...	3.08 ± 0.08	2.36 ± 0.07
$N^{*}_{H,z}$ (10^{21} atom cm^{-2}).....	...	$6.01^{+0.59}_{-0.52}$	$9.54^{+0.64}_{-0.66}$
A^{I}_{z} (10^{-5} photons cm^{-2} s^{-1})	...	$5.10^{+1.57}_{-2.54}$	$6.80^{+1.43}_{-1.91}$
χ^2_r (dof).....	...	770 (726)	655 (615)
E. Variable Covering Fraction and A_{pl}			
A_{pl} (10^{-3} keV cm^{-2} s^{-1} keV^{-1}).....	...	3.26 ± 0.08	2.28 ± 0.07
C_{XSTAR}[b] (%).....	...	97 ± 65	33^{+39}_{-33}
A^{I}_{z} (10^{-5} photons cm^{-2} s^{-1})	...	$2.32^{+1.30}_{-2.00}$	$7.73^{+1.51}_{-2.21}$
χ^2 (dof).....	...	801 (726)	656 (606)

NOTE.—Errors are for $\pm$90% confidence for one interesting parameter ($\chi^2_{min} + 2.71$)

[a] Lower bound set to 0.176×10^{21} cm^{-2}.

[b] Covering fraction as defined in eq. (A2).

(Tanaka et al. 1995). We use the parameterization described in Fabian et al. (1989), with the line emissivity varying as $r^{-2.5}$ over the region $3r_S < r < 1000r_S$, where r_S is the Schwarzschild radius of the putative central black hole. We constrained the energy of the line to lie in the range 6.4–6.9 keV. This fit yielded a line with an equivalent width of 456 ± 100 eV and a rest-frame centroid energy $E^{I}_{z} = 6.40(<6.55)$ keV. The inclination angle of the disk was implied to be $i = 28^{+10}_{-20}$ degrees and the χ^2 statistic was 847 for 773 dof. While we cannot statistically distinguish between a broad Gaussian line and that expected from a relativistic disk in this case, we note that when a simple symmetric Gaussian line is fitted to the data, we always observe an excess of counts over the model, between 5 and 6 keV, suggestive of a red wing in the line profile.

4.2. *The Spectral Variability*

The warm absorber/emitter model was also applied to the high and low state spectra. Unfortunately, however, because of the relatively low signal-to-noise ratio of the datasets, the best-fitting solutions offer no insight into the origin of the spectral variability when all parameters are allowed to be free (Table 2A).

Given the trade-off between continuum and absorption parameters, we proceeded to fix parameters in turn (at the best-fit values obtained for the mean spectrum) in an attempt to determine whether the spectral variability could be described by a simple variation in just one of the model parameters. Because the iron Kα line is thought to be predominantly produced in a region distinct from the warm

absorber, it was allowed to be free in these fits. Tables 2B–2E tabulate the variable parameters in each fit, with the exception of the iron Kα line energy and width, which were found to be consistent with the mean spectrum in each fit (although the line normalization shows marginal evidence for variability, and therefore is tabulated). We find:

1. *Variable* Γ *and* $A_{\rm pl}$ (*Table 2B*).—This model adequately describes the spectral variability, with the power-law index changing from 1.94 ± 0.03 to 1.79 ± 0.03 as the power-law normalization ($A_{\rm pl}$) fell by $\sim 60\%$. The constraint on current models implied by this scenario is that they must be able to produce a flattening of continuum shape by $\Delta\Gamma = 0.15$ on a timescale of 50,000 s. This possibility is discussed in § 6.

2. *Variable* ξ *and* $A_{\rm pl}$ (*Table 2C*).—This model provides a simple explanation of the observed spectral variability: a drop of $\sim 25\%$ in the normalization of the power-law component is accompanied by a 40% drop in the gas ionization parameter on a timescale of $\sim 50{,}000$ s. The implications of this are also discussed in § 6. We also note that, under this scenario, there is marginal evidence for an increase in the intensity of the iron line between the high and low states.

3. *Variable* $N^{*}_{{\rm H},z}$ *and* $A_{\rm pl}$ (*Table 2D*).—The observed spectral variability can be explained by a 60% increase in column, correlated with a $\sim 30\%$ drop in power-law normalization. This scenario requires coincidental variations of column (by, for instance, transverse motion across the line of sight) and continuum. This appears contrived, and we do not discuss it any further.

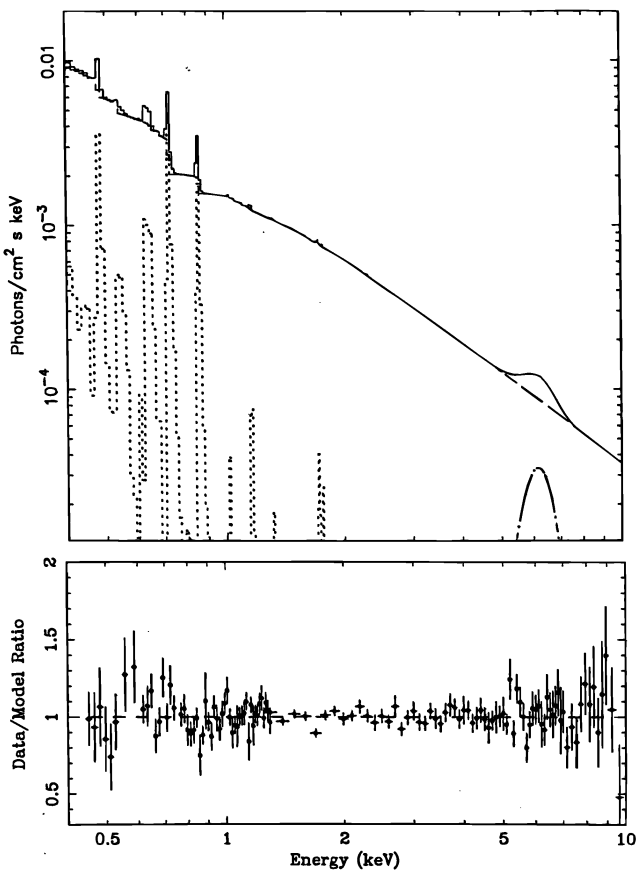

FIG. 4.—(*Top panel*) Best-fit model to the mean spectrum using the XSTAR warm absorber model (Table 2A). (*Bottom panel*) Corresponding data/model ratio.

4. *Variable* $C_{\rm XSTAR}$ *and* $A_{\rm pl}$ (*Table 2E*).—This model suggests a drop of $\sim 30\%$ in power-law normalization. However, for both the high and low states, the covering fraction is poorly determined and the relationship between the two variable quantities is unclear. While there is evidence that the iron Kα line increased significantly between the high and low states, this model yielded the worst fits to both spectra, and we consider it no further.

5. X-RAY REFLECTION FROM IONIZED MATERIAL

The presence of the strong iron Kα line suggests that a part of the primary X-ray radiation is most likely reprocessed by optically thick gas out of the line of sight. As shown recently by Życki & Czerny (1994), if this gas is partially ionized, then the resultant iron line can have equivalent widths larger than the usual "cold" case[5] by a factor of 3–4. Moreover, many spectral features, both in emission and absorption, can appear in the soft X-ray band as a result of such reprocessing (e.g., Ross & Fabian 1993; Życki et al. 1994).

The reprocessing material, out of the line of sight, is commonly considered to be associated with the putative accretion disk. Życki et al. (1994) calculate the spectrum of radiation reprocessed by a partially ionized, optically thick medium illuminated from above by an ionizing continuum (often referred to as the "reflected" spectrum). Such a model predicts spectral features similar to those observed in Mrk 290; hence, we apply that model to these data. The model calculations consist of radiative transfer and photoionization. The former is calculated by employing a Monte Carlo method in a plane-parallel geometry with constant density, but allowing for vertical changes of gas temperature and opacity. It is assumed that in addition to the irradiating continuum there is soft thermal radiation representing the internal energy generation within the material. This is modeled as a blackbody with the temperature (10^5 K) constant with depth, which has the effect of lowering the local Compton temperature and providing a minimum for the local gas temperature. The photoionization calculations again utilize the XSTAR code, in this case assuming a hydrogen density $n = 10^{14}$ cm^{-3}. (Further details of the model can be found in Życki et al. 1994.)

As in § 4, the model spectra are parameterized by the ionization parameter $\xi_{\rm ref} = 4\pi F_h\, dE/n$, but in this case F_h is defined as the integral over 0.1–100 keV, as opposed to the integral over 1–10^3 Ry, as used above.[6] Besides the different geometry and the higher gas density assumed, the only other significant difference between the optically thick reflector models discussed here and the optically thin warm absorber/emitter model discussed in the previous section is that here we allow the spectral index of the ionizing continuum to be a free parameter in the fits.

We have constructed a grid of models parameterized by Γ and $\xi_{\rm ref}$. These models include strong iron emission (and therefore no additional Gaussian profile is included to model the iron K regime, as in the previous section). Table 3 contains the results of these fits. In order to fit the overall spectral shape, we require the power-law continuum com-

[5] Obviously an overabundance of iron (compared to cosmic abundances) will also increase the Kα equivalent width (George & Fabian 1991).

[6] We use the different definitions here in order to be consistent with the original works.

TABLE 3

IONIZED REFLECTOR FITS TO THE *ASCA* OBSERVATION OF MRK 290

Parameter	Mean	High State	Low State
A. Power Law with Ionized Reflector			
A_{pl} (10^{-3} keV cm^{-2} s^{-1} keV^{-1}).....	$2.16^{+0.05}_{-0.10}$	2.54 ± 0.07	$1.77^{+0.05}_{-0.13}$
Γ.....	$1.77^{+0.01}_{-0.04}$	$1.78^{+0.02}_{-0.05}$	$1.73^{+0.02}_{-0.05}$
$N_{H,0}$[a] (10^{21} atom cm^{-2})	$0.176 < 0.26$	$0.176 < 0.36$	$0.176 < 0.55$
$N_{H,z}$ (10^{21} atom cm^{-2}).....	$1.60^{+0.16}_{-0.30}$	$1.00^{+0.18}_{-0.39}$	$1.85^{+0.20}_{-0.58}$
$\mathscr{R} \equiv A_{ref}/A_{pl}$	$3.4^{+0.4}_{-0.5}$	$2.5^{+0.4}_{-0.6}$	$4.1^{+1.4}_{-0.6}$
ξ_{ref} (ergs s^{-1} cm)	82^{+14}_{-10}	71 ± 17	69^{+15}_{-8}
χ^2 (dof).....	867 (788)	780 (725)	663 (614)
B. Variable Γ and A_{pl}			
A_{pl} (10^{-3} keV cm^{-2} s^{-1} keV^{-1}).....	...	2.67 ± 0.07	1.71 ± 0.06
Γ.....	...	1.84 ± 0.02	1.70 ± 0.03
χ^2 (dof).....	...	797 (729)	665 (618)
C. Variable $\mathscr{R}$ and A_{pl}			
A_{pl} (10^{-3} keV cm^{-2} s^{-1} keV^{-1}).....	...	2.58 ± 0.06	1.80 ± 0.05
$\mathscr{R}$	...	3.0 ± 0.3	3.3 ± 0.4
χ^2 (dof).....	...	819 (792)	688 (618)
D. Variable $N_{H,z}$ and A_{pl}			
A_{pl} (10^{-3} keV cm^{-2} s^{-1} keV^{-1}).....	...	2.46 ± 0.06	1.86 ± 0.06
$N_{H,z}$ (10^{21} atom cm^{-2}).....	...	1.15 ± 0.14	2.10 ± 0.22
χ^2 (dof).....	...	799 (729)	673 (618)
E. Variable ξ_{ref} and A_{pl}			
A_{pl} (10^{-3} keV cm^{-2} s^{-1} keV^{-1}).....	...	2.55 ± 0.06	1.82 ± 0.06
ξ_{ref} (ergs s^{-1} cm)	...	$79.0^{+7.6}_{-6.3}$	$68.8^{+11.8}_{-9.8}$
χ^2 (dof).....	...	823 (729)	685 (618)

NOTE.—Errors are for $\pm$90% confidence for one interesting parameter ($\chi^2_{min} + 2.71$)

[a] Lower bound set to 0.176×10^{21} cm^{-2}.

ponent, but not the reflected spectrum, to be absorbed by a column of cold material intrinsic to the AGNs.

5.1. *The Mean Spectrum*

The results of this fit are listed in Table 3A, and the best-fit model is shown in Figure 5 along with the data/model ratio. In Table 3, we use the quantity $\mathscr{R}$, which is the ratio of the normalization of the flux of the power-law component at 1 keV to that of the reflected spectrum for a semi-infinite slab. This ratio is a measure of the solid angle subtended by the reprocessing material, normalized to 2π.

Comparison of Figures 2 and 5 illustrates the overall improvement in fit obtained by the application of such a model. However, a comparison of Figures 4 and 5 reveals that the reflection model does not completely explain the soft X-ray emission features below 0.7 keV. It is unclear whether the excess in the data/model ratio in the 0.5–0.6 keV regime is caused by a deficit of line emission or an excess of absorption in the model compared to the data. The poorness of fit at the softest energies implies that both the iron Kα line and soft X-ray features cannot be explained with a single ionization state reflection model. We also note that once again there is a deficit in the ratio close to 1.7 keV, which arises as a result of the model prediction of significant silicon line emission in excess of that observed (a similar but less significant deficit is seen at $\sim$2.4 keV, attributable to sulphur).

5.2. *The Spectral Variability*

While the reflection model did not fit all of the soft X-ray emission features, it does appear to fit the overall continuum shape quite well. Thus, we proceeded to investigate the spectral variability in the context of this model.

Again we applied the model to the high and low state spectra in turn and found that, if we allowed all parameters to be free, then no insight is obtained into the origin of the spectral variability (Table 3A). Thus, we repeated the procedure of examining the possibilities of a simple solution based on variability in only one of the spectral components:

1. *Variable* Γ *and* A_{pl} (*Table 3B*).—This model adequately describes the spectral variability, with the power-law index changing from 1.84 ± 0.02 to 1.70 ± 0.03 as the power-law normalization fell by $\sim$40%. This is discussed in § 6.

2. *Variable* $\mathscr{R}$ *and* A_{pl} (*Table 3C*).—When all other parameters are fixed, the relative normalization of the power law and reflected components do not change significantly and the fits are poor. Thus, this cannot be the origin of the observed spectral variability, and we discuss this possibility no further.

3. *Variable* $N_{H,z}$ *and* A_{pl} (*Table 3D*).—While the observed spectral variability can be explained by a factor of almost 2 increase in the cold absorbing column—correlated with a 25% drop in power-law normalization—it is again unlikely

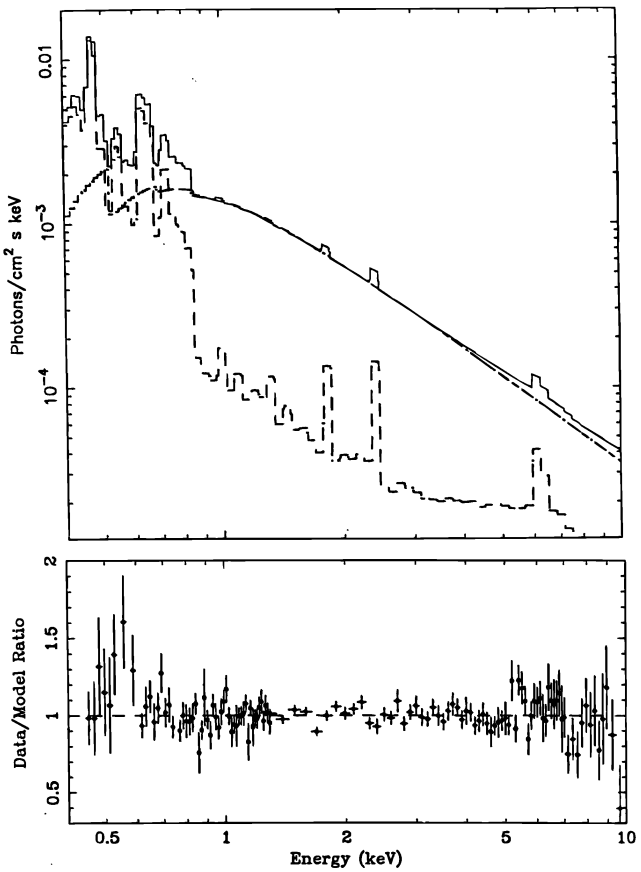

FIG. 5.—(*Top panel*) Best-fit model to the mean spectrum using the Reflection model (Table 3A). We note that in this model the recombination continua are Comptonized during their passage out of the slab and therefore are less apparent in the emergent spectrum than for the warm absorber/emitter model. (*Bottom panel*) Corresponding data/model ratio.

that these two parameters are physically linked, and this possibility is discussed no further.

4. *Variable* $\xi_{\rm ref}$ *and* $A_{\rm pl}$ (*Table 3E*).—This model provides a relatively poor fit to the high- and low-state data, and the best-fit values of $\xi_{\rm ref}$ are consistent with each other for the two flux states. Thus, variations in $\xi_{\rm ref}$ do not appear to be a good explanation for the observed spectral variability. We return to this point in § 6.

6. DISCUSSION

6.1. *Interpretation of the Warm Absorber/Emitter Results*

In § 4, we found that the warm absorber/emitter model can provide an explanation for the *ASCA* observation of Mrk 290. Unfortunately, however, the signal-to-noise ratios of the spectra are insufficient to allow us to determine a unique explanation for the origin of the spectral variability observed between the high and low states. Nevertheless, we found two physically plausible explanations for the variability to be consistent with the data: variations in both flux and spectrum of the ionizing continuum (Table 2B), and a variation in just the normalization of the continuum along with a correlated change in the ionization state of the line-of-sight absorber (Table 2C).

Before proceeding to discuss the implications of the data, we first review a number of specific predictions about the response of the reprocessor to variations in the incident continuum implied by the assumptions used in the model.

By rearranging the definition of ξ (eq. [A3]) using the fact that $N^*_{{\rm H},z} = n\Delta r$ (where Δr is the thickness of the ionized shell), we obtain

$$\Delta r = \frac{\xi N^*_{{\rm H},z} r^2}{L_s}, \tag{1}$$

where r is the radius of the shell (centered on the ionizing source), and L_s the luminosity of the central ionizing continuum (in the 1–10^3 Ry band). If it is in equilibrium, then the warm absorber/emitter must lie along this relationship in the r–Δr plane. Additional constraints can be imposed by supposing that the success of XSTAR in fitting the data is a consequence of the underlying assumptions being correct. Our assumptions are as follows:

1. The plane-parallel geometry assumed for the XSTAR model requires that the thickness of the ionized shell be smaller than its radius (i.e., $\Delta r/r \leq 1$). From equation (1), this leads to a maximum radius $r^{\rm geo}_{\rm max}$ of the ionized shell (e.g., Turner et al. 1993) of:

$$r^{\rm geo}_{\rm max} = \frac{L_s}{N^*_{{\rm H},z}\xi}. \tag{2}$$

2. In order that time-dependent photoionization models are not necessary, we require the following: (*a*) The atomic timescales within the reprocessor should be shorter than both $t_{\rm var}$ and the light travel time through the shell ($t_{\rm lt} = \Delta r/c$), and therefore the ionized material can achieve equilibrium. One of the most important atomic timescales is the recombination timescale ($t_{\rm rec}$), and Reynolds & Fabian (1994) state that for an element of atomic number Z,

$$t^Z_{\rm rec} \sim 3 \times 10^8 Z^{-2} T_e/n_e \ {\rm s}\ ; \tag{3}$$

where T_e is the electron temperature, and n_e the electron density in the ionized material. (*b*) The shape of the ionizing continuum should be constant on timescales of at least $t_{\rm var}$. (*c*) The time scales affecting the geometric distribution of the ionized gas (in both the radial and transverse directions) must be longer than $t_{\rm var}$, so that the gas "stays put" during continuum variations. (*d*) In areas of parameter space in which the emitted spectrum is important, the light travel time to the shell should be less than $t_{\rm var}$, so the parts of the shell out of the line of sight will be at the same ionization state as implied by the absorption spectrum along the line of sight. Thus, if we observe correlated changes in the emission and absorption properties of the shell, we require the radius of the shell to be within a maximum of

$$r^{\rm lt}_{\rm max} = t_{\rm var}\, c \tag{4}$$

(assuming this condition is satisfied, the requirement that $\Delta r/r < 1$ implies that the light travel time through the shell will also be smaller than $t_{\rm var}$).

Of these assumptions, only item 2(a) and the necessity for 2(d), can be tested ex post facto (see below). The ionization state of the material is dominated by the ionizing continuum in the EUV/XUV band; thus item 2(b) can only be tested using simultaneous observations in these bands, unfortunately unavailable for the observation of Mrk 290 presented here. There are no compelling dynamical arguments requiring item 2(c) to be valid, although observations of other Seyfert galaxies in which variable absorption is

uncorrelated with continuum luminosity changes can provide severe tests for dynamical models (e.g., Reynolds & Fabian 1994).

There are also a number of constraints that lead to a minimum on the radius of the shell. Certainly, we expect the shell to be outside the innermost stable orbit of the central black hole and therefore to have a radius $r > 3r_s = 9 \times 10^{11} M_6$ cm in the Schwarzschild case (where M_6 is the mass of the hole in units of $10^6 M_\odot$). In order that the fits listed in Table 2B–2E (in which the parameters of the emitted spectrum [only] are held constant between the high and low states) are valid, we require that assumption 2(d) is not valid and therefore $r \gtrsim 1.5 \times 10^{15}$ cm.

We now return to the spectral analysis of our Mrk 290 observations presented in § 4. First, we consider the implications of the results obtained for the high and low states when the normalization of the ionizing continuum ($A_{\rm pl}$) and ionization parameter (ξ) were allowed to vary, but all other parameters were fixed at the mean state values (Table 2C). As described above, such a model provides a viable explanation for the variability, with a near doubling in $A_{\rm pl}$ leading to a similar change in ξ—exactly the behavior expected from a warm absorber/emitter. From equation (1), with $N^*_{{\rm H},z} = 8 \times 10^{21}$ cm^{-2} (Table 2A) and the values of ξ and L_s ($\sim 5 \times 10^{43}$ ergs s^{-1}) given in Table 2C, we have $\Delta r \sim 4 \times 10^{-21} r^2$ cm and $r \leq r^{\rm geo}_{\rm max} \simeq 3 \times 10^{20}$ cm (eq. [2]). Using equation (3), assuming $n = n_e$ and equating T_e to the mean gas (ion) temperature ($T \sim 10^5$ K), $t_{\rm rec} \sim 5 \times 10^{11} n^{-1}$ s for the most important coolants (carbon, oxygen, and neon). Thus, the requirements that $t_{\rm lt} > t_{\rm rec}$ requires that $n \gtrsim 10^7$ cm^{-3}, consistent with our XSTAR models. For values on $N^*_{{\rm H},z}$ found for Mrk 290, this leads to an upper limit on the shell thickness of $\Delta r = N^*_{{\rm H},z}/n \leq 7 \times 10^{14}$ cm and therefore (eq. [1]) $r \leq 5 \times 10^{17}$ cm.

An alternative explanation for the spectral variability observed in Mrk 290 was presented in § 4. In this scenario, the difference between the high and low state epochs is simply owing to variations in the ionizing continuum (in both flux and spectral index; Table 2B), with the parameters of the warm absorber/emitter held constant. This explanation is at odds with our simple models. The data are consistent with changes in the ionizing continuum—with the photon index changing by $\Delta\Gamma \sim 0.15$—with no observable change in the warm absorber/emitter. The only way to account for this scenario in the context of our XSTAR models is if the ionized material is not in fact at equilibrium because of one of the atomic timescales being longer than $t_{\rm var}$. In this case, the transmission opacity and emission spectrum merely represents a time-averaged ionization state. Reversing the argument above, this requires $n \lesssim 10^7$ cm^{-3}. We note that the constraint that $r \leq r^{\rm geo}_{\rm max}$ is only violated for extremely low density gas, $N \lesssim 40$ cm^{-3}. We cannot further distinguish between this possibility and the one discussed in the previous paragraph.

6.2. *Interpretation of the Ionized Reflector Results*

The reflection model is interesting because it can potentially provide a self-consistent description of the strength of the iron K-shell emission line and the soft X-ray spectral features. However, this model component predicts a stronger softening of the spectrum below ~ 1 keV than observed in Mrk 290. Thus, in order to fit the overall spectral shape in § 3, a column of cold material was added to the model, absorbing the power law but not the reflected component. Physically, such a parameterization may be reconciled with a model in which part of the continuum radiation is blocked from view, perhaps by a cloud of gas covering the central source. Since the reflected continuum is dominated by the region of the slab with $r/h \sim$ a few—where h is the height of the primary source above the reprocessing slab (George & Fabian 1991)—the cloud must be smaller than $\sim h$.

Overall, the fit is not as good as that provided by the warm absorber/emitter in Table 2. Figure 5 shows that this is predominantly because the detailed structure of the spectral features is better described by the warm absorber/emitter than the reflection model. The reflection model is constrained to simultaneously explain the iron Kα line and the soft X-ray regime in a simple way. From our analysis, we conclude that the data are not consistent with both of these sets of lines being produced from the same region of an ionized reflector. Of course, the warm absorber/emitter model cannot explain both hard and soft X-ray regimes either, and it is only successful when a broad emission line is added to the model to explain the iron Kα line. The warm absorber/emitter scenario suggests that the iron K line is broad. In the reflection model, however, the iron K regime includes emission from appropriate ionization states of iron Kα, Kβ, and iron K absorption. Inclusion of the features can mimic a broad-line profile in low signal-to-noise data.

As shown in Tables 3C–3E, the spectral variability is not well explained by a simple response of the reflector to a change in ionizing flux. Again, we can explain the spectral variability by continuum slope variations, while the reflected spectrum remained constant (Table 3B). This model is reasonable if there is a time lag between the primary continuum and reflected spectrum. In this case, the lag is greater than 50,000 s and therefore the separation of the two must be $h > \sim 10^{15}$ cm ($10^4 r_s$ for a $10^6 M_\odot$ black hole), somewhat difficult to reconcile with the relatively high ionization parameter.

In all the ionized reflector fits we obtain values of $\mathscr{R} > 2$, indicating either that the ionizing continuum is anisotropic (i.e., that the luminosity in the direction of the reflector exceeds that directed towards us), or that there is a significant time lag ($> t_{\rm var}$) between the primary source and reflector.

6.3. *A Hybrid Model*

The difficulty in explaining the soft X-ray emission lines and the iron Kα using the reflection model led us to consider one further possibility involving reflection from ionized material, as before, with both the primary continuum and reflected spectrum suffering attenuation through the warm absorber/emitter, from § 4 (instead of the primary continuum being absorbed by cold material as described above). While complex, this model is interesting since it is reasonable to expect some contribution to the observed spectrum from reprocessors both in and out of the line of sight. Indeed, observations of other Seyfert galaxies has shown strong evidence that reprocessing from both locations is important (e.g., Nandra & Pounds 1994 and references therein).

When this hybrid model was applied to the data, the fit to the soft X-ray regime was dominated by the warm absorber/emitter, while the iron Kα region was well fit by the reflection component. Consequently, the best-fitting parameters for the warm absorber/emitter were not significantly different from those presented in Table 2 (and there-

fore are not tabulated again). Overall, the fit to this complex model yielded $\chi^2 = 857$ for 789 dof (slightly worse than the fit in Table 2, because the iron Kα line is constrained to be part of the reflection spectrum rather than an arbitrary Gaussian line). The removal of the requirement that the reflection component simultaneously explains both the soft and hard X-ray features yields a preferred origin for the iron line from relatively low ionization state material ($\xi_{\rm ref} = 20^{+7}_{-20}$). Again we find a high value of $\mathscr{R}$, perhaps implying enhanced emission of the continuum toward the reflector. A possible mechanism for such an enhancement involves inverse Compton scattering of an anisotropic radiation field (Ghisellini et al. 1991).

The spectral variability is dominated by changes below 2 keV. As the warm absorber/emitter dominates the fit in that regime (with parameters consistent with those presented in Table 2), the conclusions on the origin of the spectral variability were also consistent with those presented in Table 2, and therefore the analysis of spectral variability is not repeated here.

7. CONCLUSIONS

Our *ASCA* observation of Mrk 290 has revealed a complex spectrum in the 0.4–10 keV band, with strong emission and absorption features superimposed on a power-law continuum. The features below $\sim$2 keV indicate that reprocessing in ionized material is important in this source. These soft spectral features, along with strong iron Kα emission and significant flux-correlated spectral variability, make this source a good test of reprocessing models.

The spectral variability could be explained as a variation in the flux and index of continuum alone. However, the reprocessing material is highly ionized and therefore most likely close to the continuum source. Thus, it is more compelling to try and relate the spectral variability to changes in the reprocessing material that result from variations in the ionizing flux.

In this paper, we have considered two reprocessing models based on the XSTAR photoionization code (1) for a warm absorber/emitter along the line of sight, and (2) for an ionized reflector out of the line of sight. We also briefly consider a hybrid model consisting of both components.

We find the warm absorber/emitter model provides a good explanation of the overall spectral shape, with an underlying power-law ($\Gamma \sim 1.9$) continuum passing through a column density of $N^*_{{\rm H},z} \sim 8 \times 10^{21}$ cm^{-2} of ionized material ($\xi = 24$) most likely within $\sim 10^{17}$ cm of the central source. While the data do not allow us to unambiguously determine the origin of the spectral variability, it is consistent with a drop of $\sim$25% in flux accompanied by a proportional drop in the ionization state of the warm absorber. This model cannot explain the intense ($\sim$500 eV equivalent width) Kα line present in the source. Modeling the line as a Gaussian, we find its energy consistent with an origin in neutral material and a FWHM indicative of velocities of $\lesssim 0.01c$. We also found the line profile to be consistent with that expected from the inner regions of a relativistic accretion disk, at an inclination of $\sim 30°$.

We find the ionized reflector can also model the overall spectral shape, yielding $\xi_{\rm ref} \sim 80$, although it has some difficulty simultaneously fitting both the iron Kα and soft X-ray emission features. This model offers no simple explanation for the observed spectral variability, and the intensity of the reflected component is greater than that expected from a semi-infinite slab illuminated by an isotropic source.

We applied a hybrid model featuring reprocessing in both the warm absorber/emitter and reflector. In this case, the preferred fit models the soft X-ray regime (and spectral variability) with the warm absorber/emitter and the iron Kα line with a weakly ionized reflector ($\xi \lesssim 20$). We believe this hybrid model is the most realistic representation of the innermost regions of Mrk 290 and other Seyferts.

We thank Hagai Netzer and Richard Mushotzky for useful discussions, and Paul Nandra for help with the figures. T. J. T., I. M. G., and T. Y. acknowledge the financial support of the Universities Space Research Association. The work of P. T. Z. was supported in part by grant 2P30401004 of the Polish State Committee for Scientific Research. This research was performed using XSELECT (version 1.0h), XSPEC (version 9.0), and XSTAR version 1.19. We made use of the Simbad database, operated at CDS, Strasbourg, France, as well as data obtained through the HEASARC on-line service provided by NASA/GSFC.

APPENDIX

In this section, we briefly summarize the most important aspects of our XSTAR (version 1.19) models. Further details can be found in Kallman & Krolik (1995).

Each XSTAR run consists of a plane-parallel slab of gas illuminated by an ionizing continuum. The code simultaneously determines the ionization state of the gas and the local radiation field as a function of position in the slab. The state of the gas is defined by its temperature and by the ion abundances. All ions are predominantly in the ground state, and except for hydrogen and helium, the populations of excited levels are neglected. The relative abundances of the ions of a given element are found assuming a local balance between ionization and recombination, subject to the constraint of particle number conservation for each element. The ionization balance is affected by a variety of physical processes, most notably photoionization, and radiative and dielectronic recombination. The temperature is found by solving the local equation of thermal equilibrium, equating the net heating of the gas caused by absorption of incident radiation with cooling caused by emission by the gas. These rates are derived from integrals over the absorbed and emitted radiation spectra. Although Compton scattering is not explicitly included as a source or sink of radiation, its effect is included in the calculation of thermal balance.

Rates for atomic processes involving electron collisions have been modified since the publication of Kallman & McCray (1982) in order to be consistent with those used by Raymond & Smith (1976). Recombination and ionization rates for iron have been updated to those of Arnaud & Raymond (1992). In addition, we have added many optical and UV lines from ions of medium-Z elements (C, N, O, Ne, Si, and S) using collisional and radiative rates from Mendoza (1982). The elements Mg, Ar, Ca, and Ni have also been added. The current model has a total of 168 ions producing 1715 lines, of which 665 have energies

greater than 120 eV (10 Å) and approximately 800 are resonance lines. For each ion we also calculate the emission from radiative recombination onto all the excited levels that produce resonance lines. The number of such continua is equal to the number of resonance lines in the calculation. We assume the following abundances:

$$(\mathrm{H{:}He{:}C{:}N{:}O{:}Ne{:}Mg{:}Si{:}S{:}Ar{:}Ca{:}Fe{:}Ni}) = (1{:}0.1{:}3.7\times10^{-4}{:}1.1\times10^{-4}{:}6.8\times10^{-4}{:}2.8\times10^{-5}{:}$$
$$3.5\times10^{-5}{:}3.5\times10^{-5}{:}1.6\times10^{-5}{:}4.5\times10^{-6}{:}2.1\times10^{-6}{:}2.1\times10^{-6}{:}2.5\times10^{-5}{:}2\times10^{-6}).$$

The output from each model consists of the continuum spectrum emitted in the forward direction and the spectrum transmitted through the slab. The emitted spectrum (which, at most, represents half of the total energy radiated by the clouds) includes continuum emission by bremsstrahlung and recombination as well as line emission by a variety of processes, including recombination, collisions, and fluorescence following inner shell photoionization. Line transfer is treated using an escape probability formalism, including the effects of line destruction by collisions and continuum absorption. Transfer of the continuum is calculated using a single stream approximation, as described in Kallman & McCray (1982). The entire slab structure is iterated several times in order to enable an accurate treatment of the photon escape from the unilluminated face of the slab. Experience has shown that the relevant optical depths converge to within 10% after three iterations for most values of ionization parameter and column density.

The emitted spectrum does not include the incident continuum, but it does include the lines and recombination continua emitted by the slab. This quantity is produced as part of the standard XSTAR output as the specific luminosity (in ergs s^{-1} erg^{-1}) at the unilluminated cloud face. This quantity can be expressed in terms of the efficiency of reprocessing of the incident continuum photons into lines and recombination continua, f_ϵ, the ionizing luminosity of the illuminating source, L_s (between 1 and 1000 Ry), as $L_\epsilon = L_s f_\epsilon$. In fitting to data, XSPEC uses the F_n, defined as the photons cm^{-2} bin^{-1} s^{-1} incident on the detector. This is related to the quantity produced by XSTAR by

$$F_n = \frac{\Delta\epsilon}{\epsilon}\frac{L_s f_\epsilon}{4\pi D^2} C_{\mathrm{XSTAR}} , \tag{A1}$$

where D is the distance to the source, C_{XSTAR} is the covering fraction of the gas, and $\Delta\epsilon/\epsilon$ is the fractional energy width of the energy bins. In our fits, we adopt the fiducial values for these quantities, $L_s = L_{46}\,10^{46}$ ergs s^{-1}, $C = 1$, and $D = D_{\mathrm{Mpc}}$ Mpc. Values of the fitted normalization A_{XSTAR} are related to these quantities by

$$A_{\mathrm{XSTAR}} = C_{\mathrm{XSTAR}}\, L_{46}\, D_{\mathrm{Mpc}}^{-2}/(4\pi) . \tag{A2}$$

We also use the transmission coefficient of the models, i.e., the fraction of the incident continuum that traverses the cloud without suffering photoelectric absorption as a function of energy; this represents the warm absorber. A grid of model spectra were produced for a range of $N^*_{\mathrm{H},z}$ and ionization parameter

$$\xi = 4\pi F_s/n , \tag{A3}$$

where F_s is the ionizing energy flux of the central source (between 1 and 1000 Ry) incident on the illuminated face, and n is the gas density. For all the runs reported here, the ionizing continuum was assumed to be a power law of photon index $\Gamma = 1.9$, and n was fixed at 10^{10} cm^{-3}. The dependence of the model results on the gas density is likely to be quite weak for densities less than $\sim 10^{14}$ cm^{-3}. The results are sensitive to the choice of ionizing power-law index but, since the continuum shape that best fits to the observed spectrum is near our adopted value, our models are not significantly deviant from self-consistency. The grid of model emission and transmission spectra were then converted to "ATABLE" and "MTABLE," respectively (Arnaud 1992), in preparation for use within the XSPEC spectral analysis package.

REFERENCES

Antonucci, R. R. J. 1993, ARA&A, 31, 473
Arnaud, K. A. 1992, OGIP memo OGIP/92-009
Arnaud, M., & Raymond, J. 1992, ApJ, 398, 394
Fabian, A. C., Rees, M. J., Stella, L., & White, N. E. 1989, MNRAS, 238, 729
Fiore, F., Elvis, M., Mathur, S., Wilkes, B., & McDowell, J. 1993, ApJ, 415, 129
George, I. M., & Fabian, A. C. 1991, MNRAS, 249, 352
George, I. M., Nandra, K., & Fabian, A. C. 1990, MNRAS, 242, 28
Ghisellini, G., George, I. M., Fabian, A. C., & Done, C. 1991, MNRAS, 248, 14
Ghosh, K. K., & Soundararajaperumal, S. 1992, MNRAS, 259, 175
Halpern, J. P. 1984, ApJ, 281, 90
Kallman, T. R., & Krolik, J. H. 1995, XSTAR manual, available at the ftp site, legacy.gsfc.nasa.gov
Kallman, T. R., & McCray, R. A. 1982, ApJS, 50, 263
Kriss, G. A., Canizares, C. R., & Ricker, G. R. 1980, ApJ, 242, 492
Kruper, J. S., Urry, C. M., & Canizares, C. R. 1990, ApJS, 74, 347
Lightman, A. P., & White, T. 1988, ApJ, 335, 57
Markarian, B. E. 1969, Astrophysics, 5, 286
Matt, G. M. 1994, MNRAS, 267, L17
Matt, G. M., Fabian, A. C., & Ross, R. R. 1993, MNRAS, 264, 839
Matt, G. M., Perola, G. C., & Piro, L. 1991, A&A, 247, 25
Mendoza, C. 1982, in Proc. IAU Symp. 103, Planetary nebulae, ed. Flower,
Morrison, R., & McCammon, D. 1983, ApJ, 270, 119
Mushotzky, R. F., Fabian, A. C., Iwasawa, K., Kunieda, H., Matsuoka, M., Nandra, K., & Tanaka, Y. 1995, MNRAS, 272, 9
Nandra, K., George, I. M., Mushotzky, R. F., Turner, T. J., & Yaqoob, T. 1995, MNRAS, 272, 9
Nandra, K., & Pounds, K. A. 1992, Nature, 359, 215
———. 1994, MNRAS, 268, 405
Netzer, H. 1993, ApJ, 411, 594
Pounds, K. A., et al. 1990, Nature, 344, 132.
Raymond, J. C., & Smith, B. H. 1976, ApJS, 35, 419
Reynolds, C., & Fabian, A. C. 1995, MNRAS, 273, 1167
Ross, R. R., & Fabian, A. C. 1993, MNRAS, 258, 189
Stark, A. A., et al. 1992, ApJS, 79, 77
Tanaka, Y., Inoue, H., & Holt, S. S. 1994, PASJ, 46, L37
Tanaka, Y., et al. 1995, Nature, 375, 659
Turner, T. J., & Pounds, K. A. 1989, MNRAS, 240, 833
Turner, T. J., Nandra, K., George, I. M., Fabian, A. C., & Pounds, K. A. 1993, ApJ, 419, 127
Wood, K. S., et al. 1984, ApJS, 56, 507
Yaqoob, T., Edelson, R., Weaver, K. A., Warwick, R. S., Mushotzky, R. F., Serlemitsos, P. J., & Holt, S. S. 1995, ApJ, 453, L81
Życki, P. T., & Czerny, B. 1994, MNRAS, 266, 653
Życki, P. T., Krolik, J. H., Zdiarski, A. A., & Kallman, T. R. 1994, ApJ, 437, 597